

Accelerated discovery via a whole-cell model

Jayodita C Sanghvi^{1,3}, Sergi Regot¹, Silvia Carrasco¹, Jonathan R Karr², Miriam V Gutschow¹, Benjamin Bolival Jr¹ & Markus W Covert¹

To test the promise of whole-cell modeling to facilitate scientific inquiry, we compared growth rates simulated in a whole-cell model with experimental measurements for all viable single-gene disruption *Mycoplasma genitalium* strains. Discrepancies between simulations and experiments led to predictions about kinetic parameters of specific enzymes that we subsequently validated. These findings represent, to our knowledge, the first application of whole-cell modeling to accelerate biological discovery.

As high-throughput experiments yield large and complex data sets, there is an increasing need for corresponding computational methods to derive knowledge from those data. Whole-cell models that incorporate every known gene function to make predictions about integrated and complex biological phenomena may address this need. In the 1980s, bacteriologists realized that the simple *Mycoplasma* spp. might be tractable for the first comprehensive description of a cell¹, and since that time several groups have worked toward building models of various aspects of *M. genitalium*, the simplest self-replicating organism^{2–4}. Most recently, members of our laboratory constructed a whole-cell model of *M. genitalium* that incorporates every known gene function to simulate a complete life cycle. The simulations generated by this model compared favorably with published data sets, which included metabolic fluxes, metabolite concentrations, growth rates, and gene and protein expression⁵.

Although these comparisons represented perhaps the broadest validation of any biological model, the most exciting promise of whole-cell modeling, prediction of previously undiscovered biology, remains to be fulfilled. In the process of model-driven discovery, for any given complex experiment, the whole-cell model can be used to produce a corresponding simulation, resulting in two sets of data, one computational and one experimental, which can be directly compared to determine how well the model describes observations. Any discrepancy between predictions and observations represents a high-probability opportunity for a discovery as the discrepancy is resolved, and new discoveries are incorporated back into the model (Fig. 1a).

We implemented this model-driven discovery approach using our whole-cell model. We compared model predictions and experimental measurements of the specific growth rates of a nonessential single-gene disruption library of *M. genitalium*, for all 86 strains for which an experimental rate could be determined^{5,6} (Fig. 1b). We also compared our predictions to a metabolic model based on flux-balance analysis⁷ and found that the whole-cell model made more quantitative predictions (Supplementary Fig. 1), underlining the need for the whole-cell model.

For 84% of the strains, the specific growth rates determined by experiment and simulation were statistically indistinguishable. Although our previous analysis showed that the model could predict the phenotypes of all 525 gene disruption strains with high accuracy ($P < 10^{-7}$)⁵, a null test applied only to the set of 86 viable strains (wherein the null hypothesis is that all viable strains grow at the same rate as the wild type) would yield a success rate of 94%. In other words, most of the viable strains grow at rates that are essentially the same as those of the wild type, and some of these are not captured by the model.

Therefore, the greatest value of this data set is found by considering the discrepancies between the model and experimental data. By combining our quantitative growth rate measurements and predictions with the qualitative information from our previous work, we produced a detailed map of model-experiment comparisons for all 525 genes in the chromosome (Fig. 1c). To our knowledge, this is the most comprehensive and quantitative comparison of any large-scale cellular model's predictions to growth-phenotype data, as other studies (including our own work) either considered only a small fraction of the total non-essential genes or else made strictly qualitative (growth or no growth) predictions^{5,8,9}.

Scrutiny of this comparison map highlighted a small group of discrepancies, the resolution of which we hypothesized would be most likely to lead to new discoveries. The model-experimental data comparisons fell into seven categories, depending on the nature of the model prediction and whether a gene's function was well-enough annotated for functional inclusion in the model (Supplementary Table 1). Two categories had the richest information content. The first group included 13 strains (Fig. 1c) for which the model could predict the qualitative essentiality but not the quantitative growth rate ($P \leq 0.01$). The second group consisted of five strains for which the model failed qualitatively, predicting a growth rate that was insufficient to sustain life ('lethal zone'; Fig. 1b); we therefore labeled the corresponding genes as 'false essential'.

For four of the 18 strains in these two categories, the difference in growth rate between model and experiment was

¹Department of Bioengineering, Stanford University, Stanford, California, USA. ²Graduate Program in Biophysics, Stanford University, Stanford, California, USA.

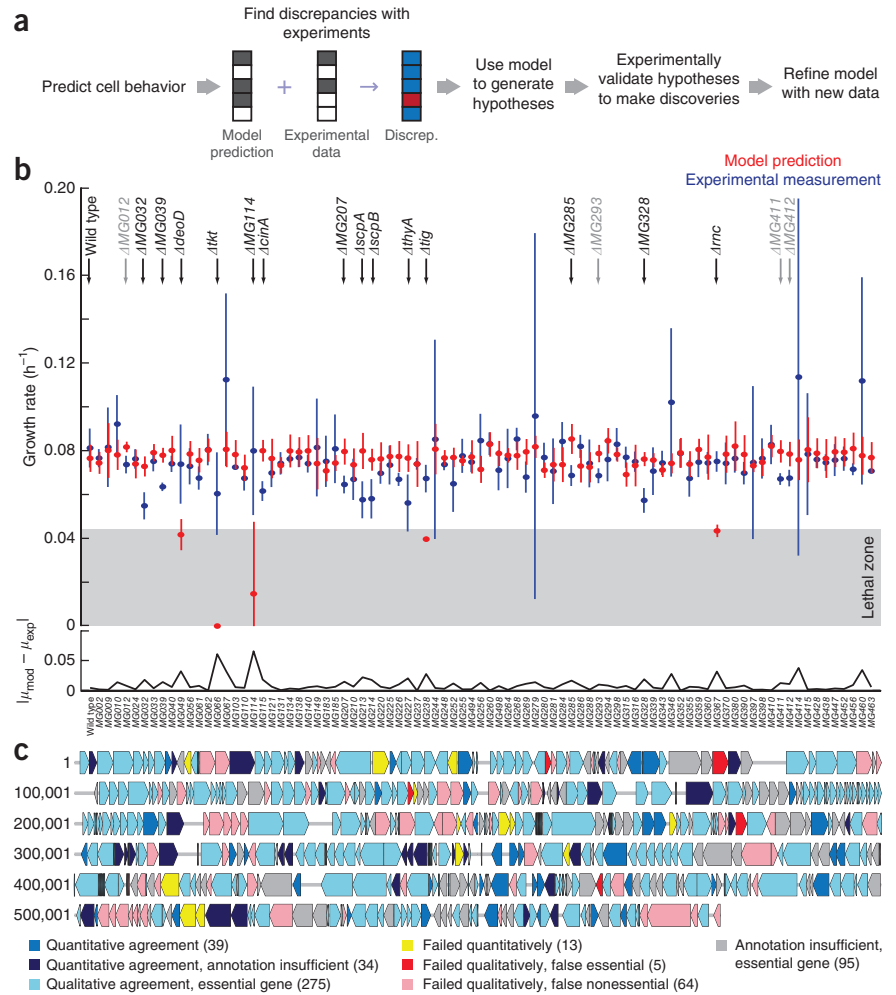
³Present address: Institute for Quantitative Biosciences, University of California Berkeley, Berkeley, California, USA. Correspondence should be addressed to M.W.C. (mcovert@stanford.edu).

Figure 1 | Model-driven discovery and the quantitative prediction of growth phenotypes.

(a) Schematic of a model-driven discovery pipeline as facilitated by a whole-cell model. (b) Simulated (model prediction, $n = 5$) and experimentally observed (two independent experiments with three technical replicates each) specific growth rates (μ) for 86 nonessential gene-disruption strains of *M. genitalium* (top). Error bars, s.d. ($n = 5$ (model) and $n = 6$ (experiment)). Absolute values of the difference between model and experiment (bottom). The 18 genes exhibiting significant (heteroskedastic two-tailed t -test and Wilcoxon rank sum test with $P \leq 0.01$, listed in **Supplementary Table 2**) model-experiment discrepancies are indicated by arrows at the top; four of these were small in magnitude (gray). Gray shading marks the 'lethal zone': five slow-growing strains that the model wrongly predicted to be nonviable. (c) Chromosome map with comparison between model predictions and experimental observations for all 525 *M. genitalium* genes. Number of genes in each category is indicated in parentheses. The 18 'false essential' genes of interest are indicated in yellow and red.

small (<20%). For the remaining 14 strains, five of the corresponding genes are associated with metabolism, two are linked to gene expression, three are involved in chromosome condensation and the remaining four genes had little or no functional annotation (**Supplementary Table 2**). For each of these genes, we explored the model's inability to predict the experimental data, looking for a possible mechanism that could explain the discrepancy. We used the whole-cell model and the literature to examine the 'molecular pathology' of each single-gene disruption, as described in our earlier work⁵. Using this analysis, we hypothesized a previously misrepresented or missing function for each of the hits for which there was a well-characterized gene annotation (**Supplementary Results** and **Supplementary Fig. 2**).

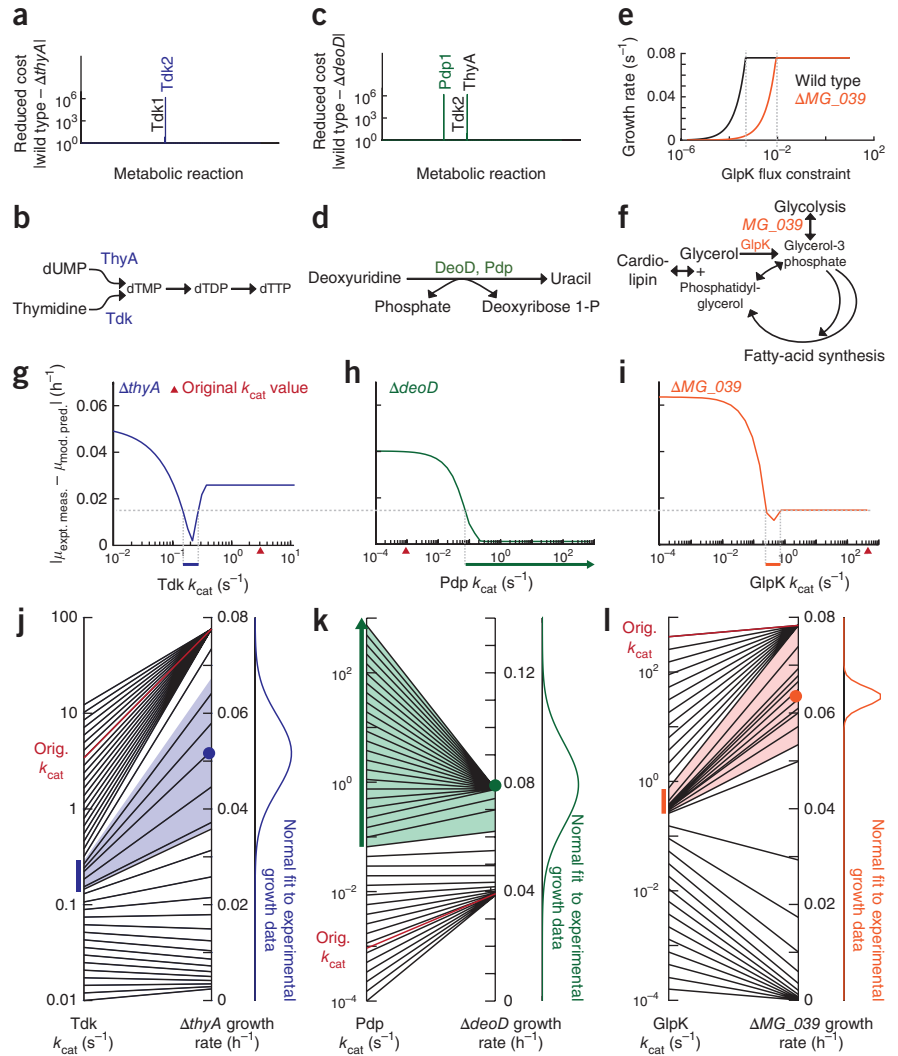
Three 'hits' were of particular interest because we could test model predictions for them using established methods. These hits were all metabolic genes: *thyA* (thymidylate synthase) and *deoD* (deoxyribose-phosphate aldolase), as previously reported⁵, and *MG_039* (glycerol phosphate). Prediction failures of the model were quantitative, not qualitative, for all three genes. (**Supplementary Table 1**). For each gene, we identified an alternate metabolic route that could compensate for its disruption. We used a strategy based on reduced costs, which are calculated as part of the metabolic submodel's linear optimization method, to determine the metabolic fluxes that according to the model were limiting cell growth¹⁰. Changing the parameter values for these fluxes would have the greatest impact on the specific growth rate calculated by the model, making them the most likely candidates for parameter estimation. For the *thyA* strain, we found only two metabolic reactions by reduced-cost analysis that did not also appear in the reduced-cost analysis of the wild-type strain (**Fig. 2a**). Both reactions were catalyzed by thymidine kinase (Tdk).



ThyA and one of the *Tdk* reactions have a common metabolic product, dTMP, which is required for DNA replication (**Fig. 2b**). Reduced-cost analysis of the *deoD* strain led to three candidate reactions, catalyzed by *ThyA*, *Tdk* and pyrimidine-nucleoside phosphorylase (*Pdp*) (**Fig. 2c**). Of these, only *Pdp* could compensate for the production of uracil by *DeoD* (**Fig. 2d**). For comparison, we performed the same reduced-cost analysis using a simple FBA framework without the additional constraints imposed by the whole-cell model. The stand-alone FBA model was unable to identify notable differences in reduced cost between the wild-type and disruption strains (**Supplementary Table 3**).

The reduced-cost analysis for *MG_039*, whose product converts dihydroxyacetone phosphate to glycerol-3-phosphate, did not highlight compensating reactions to *MG_039*. We therefore adopted a different approach, reasoning that growth of the disruption strain would be more susceptible than that of the wild-type strain to the inhibition of any candidate enzyme that could compensate for *MG_039*. We searched for metabolic reactions that, if constrained in the single-gene disruption, had a stronger effect on the calculated specific growth rate than in the wild type. Constraining glycerol kinase (*GlpK*) had the most pronounced difference in effect between the gene disruption strain and the wild type, sharply reducing the specific growth rate at a flux constraint that was over tenfold higher (**Fig. 2e**). *GlpK* catalyzes the production of glycerol-3-phosphate from glycerol as part of a complex fatty acid synthesis network with at least three interlocking

Figure 2 | The whole-cell model quantitatively predicts rate constants of metabolic reactions. **(a,c)** Reduced-cost analysis of all metabolic fluxes in the $\Delta thyA$ **(a)** and $\Delta deoD$ **(c)** single-gene disruption strains; only the notable costs are labeled. **(b,d)** Schematics of metabolic reactions that can compensate for those catalyzed by ThyA **(b)** and DeoD **(d)**. **(e)** Effect of constraining the flux of the GlpK reaction on the specific growth rates of ΔMG_039 and wild-type strains. **(f)** Reaction schematic including reactions catalyzed by the MG_039 gene product and GlpK. **(g-i)** Absolute difference between the mean model prediction (mod. pred.; $n = 6$) and the mean experimental measurement (expt. meas.; $n = 5$) of specific growth rates (μ) for the gene disruption strains $\Delta thyA$ **(g)**, $\Delta deoD$ **(h)** and ΔMG_039 **(i)** plotted against the kinetic rates of the respective enzymatic reactions. Dotted gray line indicates the cutoff for acceptable error for all strains, which was constrained by the local minimum observed in the ΔMG_039 strain. Horizontal colored bars indicate model-predicted ranges. Red triangles indicate original k_{cat} values. **(j-l)** Tdk **(j)**, Pdp **(k)**, and GlpK **(l)** k_{cat} values (left axis) to model-predicted specific growth rates of $\Delta thyA$, $\Delta deoD$ and ΔMG_039 (right axis). Colored bars indicate the k_{cat} ranges shown in **g-i**, and colored regions indicate the range of simulated specific growth rates determined by the k_{cat} range. A normal fit to the experimental specific growth-rate data is shown (right); red lines indicate original estimate of k_{cat} value used to train the model and its corresponding simulated specific growth rate.



cycles (Fig. 2f). The complexity of this subnetwork is the most likely reason for the failure of the reduced-cost analysis.

In other words, a compensating reaction existed, and was encoded in the model, for each of the three cases, yet the model failed to correctly predict the specific growth rates of the corresponding strains. We hypothesized that the failure was in the kinetic rates of the compensating enzymes. The metabolic component of the whole-cell model uses the rate of catalysis (k_{cat}), multiplied by the enzyme abundance (a dynamic variable in the model) as the upper bound of the metabolic flux for a given reaction. Many of the kinetic parameters required to build the original whole-cell model had not previously been measured in *M. genitalium* and had to be approximated from measurements in different organisms, including the parameters for Tdk, Pdp and GlpK. We therefore used the whole-cell model to determine a range for k_{cat} values for Tdk, Pdp and GlpK that would reconcile the $\Delta thyA$, $\Delta deoD$ and ΔMG_039 growth phenotypes while minimizing the effects on growth of the wild type. For each strain, we plotted the absolute value of the difference between the model-predicted and experimentally observed specific growth rates as a function of k_{cat} (Fig. 2g-i). We then examined all three plots together to determine a common difference cutoff between experimental and simulated specific growth rates. The cutoff that produced minimum discrepancy for all of the strains was 0.015 h^{-1} , which corresponds to roughly 20% of the specific growth rate of the wild type.

Implementing this cutoff, we observed a single range of k_{cat} values that minimized the discrepancy between the model and experimental measurements for each enzyme. The range for Pdp differed in that the upper limit was unbounded. We confirmed that the predicted range of k_{cat} values mapped well to the distribution of experimental measurements of growth rates of single-gene disruption strains (Fig. 2j-l).

The k_{cat} ranges, calculated directly from model predictions, were experimentally testable. We expressed the *M. genitalium* genes in *Escherichia coli*, purified the proteins and performed kinetic assays (Fig. 3a-c and Supplementary Fig. 3). The measured values corresponded well with the model's predictions and differed by at least one and up to four orders of magnitude from the values originally used to train the model (Fig. 3d). These results indicate that our model can make accurate quantitative predictions about previously unmeasured cellular properties.

As a final step in the discovery process, we incorporated all of the newly determined experimental parameters into the whole-cell model to test whether interactions between these parameters existed that might make the resulting model less predictive than expected. The new parameters led to better predictions for all strains of interest without compromising predictions of the

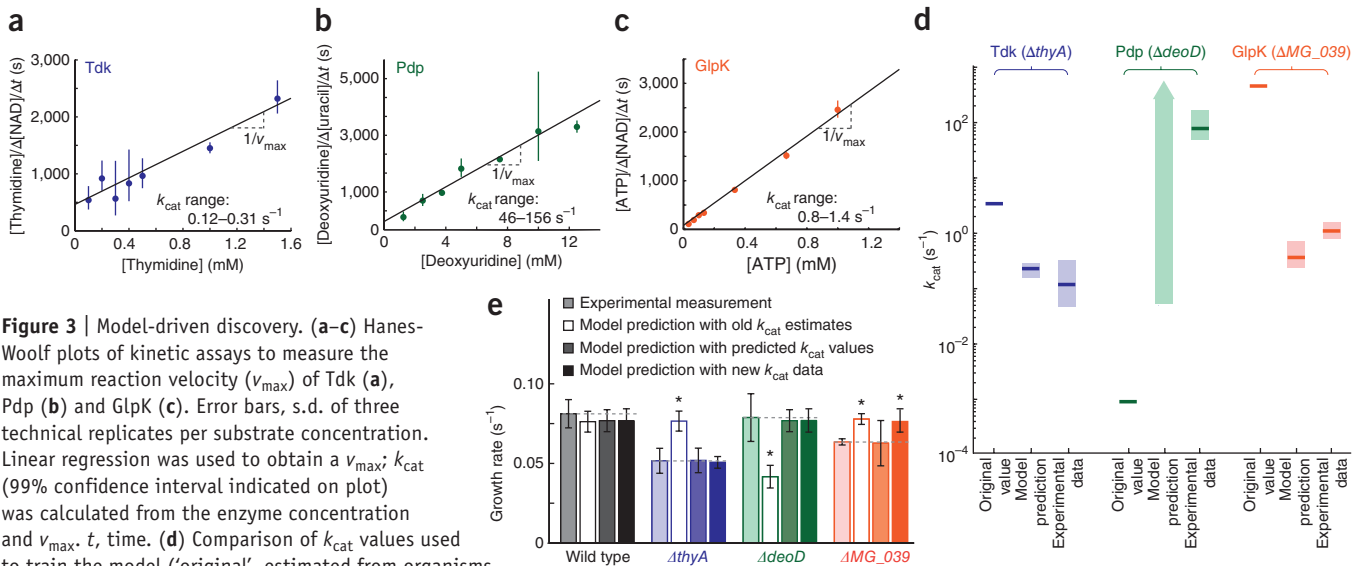


Figure 3 | Model-driven discovery. (a–c) Hanes-Woolf plots of kinetic assays to measure the maximum reaction velocity (v_{max}) of Tdk (a), Pdp (b) and GlpK (c). Error bars, s.d. of three technical replicates per substrate concentration. Linear regression was used to obtain a v_{max} ; k_{cat} (99% confidence interval indicated on plot) was calculated from the enzyme concentration and v_{max} . t , time. (d) Comparison of k_{cat} values used to train the model ('original', estimated from organisms other than *M. genitalium*), with model-based predictions and experimental measurements. (e) Predicted and measured k_{cat} values were input into the whole-cell model ($n = 6$) and compared to the experimentally measured ($n = 5$) specific growth rates and model predictions with original k_{cat} values. P values were determined by two-tailed t -test, $*P \leq 0.01$. Dashed grey lines, experimental mean. Error bars, s.d.

wild-type strain or of other single-gene disruption strains (t -test between model and experimental results, cutoff $P \leq 0.01$; Fig. 3e).

The predictions for the *MG_039* single-gene disruption strain made with the computationally derived k_{cat} value were more accurate than those made with the experimentally determined k_{cat} value. One reason for this could be that the model prediction for the enzyme concentration, which is multiplied by the k_{cat} value to determine the upper bound on the flux, is incorrect. However, we compared our model predictions for the number of proteins per cell with measurements made in the closely related *M. pneumoniae* in ref. 11 and found that the ranges of measured and predicted protein count for all three enzymes are roughly consistent with each other (Supplementary Fig. 4). Another possibility is that GlpK is not the only or most important flux-limiting enzyme, as calculated. Finally, the whole-cell model calculates the maximal rate of an enzyme as a simple product of the enzyme concentration and k_{cat} , but *in vivo* this will be determined by many other parameters and variables, from the substrate concentration and Michaelis constant (K_m) to the limits imposed by allosteric regulation and the like. One can demonstrate that a limiting concentration of intracellular glycerol would be sufficient to reduce the GlpK flux bound to the model-predicted values (Supplementary Fig. 5). A better understanding and representation of these other processes in the whole-cell model would increase its predictive power.

In summary, our whole-cell model accurately predicted multiple kinetic parameters based on growth phenotypes of single-gene disruption strains. Although encouraging, our findings represent only three instances of validation, so more work will be necessary to definitively establish the model's capacity to predict molecular properties. Nevertheless, detailed, molecular-level predictions such as we have made, based on phenotypic measurements of cellular populations, would be impossible without a comprehensive, whole-cell model that explicitly represents both molecular and cellular scales. Overall, these findings represent to our knowledge the first application of whole-cell modeling to accelerate biological discovery.

METHODS

Methods and any associated references are available in the [online version of the paper](#).

Note: Any Supplementary Information and Source Data files are available in the [online version of the paper](#).

ACKNOWLEDGMENTS

We acknowledge support from: an US National Institutes of Health Pioneer Award (5DP1LM01150-05) and an Allen Distinguished Investigator Award to M.W.C.; Siebel Scholars, US National Science Foundation and Stanford University Bio-X Fellowships to J.C.S.; an European Molecular Biology Organization Fellowship (ALTF1371-2011) to S.R.; US National Defense Science and Engineering Graduate Fellowship, US National Science Foundation fellowship, and Stanford Graduate Fellowship to J.R.K.; and Weiland and Rensselaer Engineering Fellowships to M.V.G.

AUTHOR CONTRIBUTIONS

J.C.S., J.R.K. and M.W.C. performed the simulations and computational analysis; J.C.S., S.R. and S.C. performed the enzyme expression and kinetic assays; J.C.S., J.R.K., M.V.G. and B.B. performed the growth rate measurements; J.C.S., S.R. and M.W.C. wrote the paper; and M.W.C. supervised the project.

COMPETING FINANCIAL INTERESTS

The authors declare competing financial interests: details are available in the [online version of the paper](#).

Reprints and permissions information is available online at <http://www.nature.com/reprints/index.html>.

- Morowitz, H.J. *Isr. J. Med. Sci.* **20**, 750–753 (1984).
- Suthers, P.F. *et al. PLOS Comput. Biol.* **5**, e1000285 (2009).
- Browning, S.T. & Shuler, M.L. *Biotechnol. Bioeng.* **76**, 187–192 (2001).
- Tomita, M. *et al. Bioinformatics* **15**, 72–84 (1999).
- Karr, J.R. *et al. Cell* **150**, 389–401 (2012).
- Glass, J.I. *et al. Proc. Natl. Acad. Sci. USA* **103**, 425–430 (2006).
- Orth, J.D., Thiele, I. & Palsson, B.O. *Nat. Biotechnol.* **28**, 245–248 (2010).
- Covert, M.W., Knight, E.M., Reed, J.L., Herrgard, M.L. & Palsson, B.O. *Nature* **429**, 92–96 (2004).
- Edwards, J.S. & Palsson, B.O. *BMC Bioinformatics* **1**, 1 (2000).
- Savinell, J.M. & Palsson, B.O. *J. Theor. Biol.* **155**, 215–242 (1992).
- Maier, T. *et al. Mol. Syst. Biol.* **7**, 511 (2011).

ONLINE METHODS

Single-gene disruption strain simulations and growth assays.

M. genitalium single-gene disruption and wild-type strains were obtained from J. Craig Venter Institute⁶. Specific growth rates were determined according to the colorimetric protocol described in ref. 5. Simulations were performed as described⁵. Simulation results can be found at SimTK (<https://simtk.org/home/wholecell/>). Simulated cells were modeled in an environment based on Spiroplasma 4 medium. At least six experimental replicates and five simulations were run for each disruption strain.

Protein expression. *M. genitalium* *tdk*, *pdp* and *glpK* genes were synthesized by GenScript with *E. coli* codon optimization. Genes were inserted into pGEX-6P-1 glutathione S-transferase (GST) expression vectors (GE Healthcare) by Gibson assembly¹², and sequences were verified. Resulting vectors were expressed in DH5 α *E. coli* cells. Cells were lysed by sonication, and GST-tagged proteins were pulled down using glutathione sepharose beads (GE Healthcare). Proteins were cleaved from the beads by PreScission Protease (GE Healthcare), and quantified against a BSA standard by SDS electrophoresis (Supplementary Fig. 3a–c). Final concentrations were: Tdk, 1.3 mg ml⁻¹; Pdp, 0.2 mg ml⁻¹; and GlpK, 0.14 mg ml⁻¹.

Kinetic assays. Tdk activity was measured using a spectrophotometric assay similar to that described previously¹³. Reaction schema: thymidine + ATP \leftrightarrow dTMP + ADP + H⁺ (catalyzed by Tdk); ADP + phosphoenolpyruvate + H⁺ \leftrightarrow pyruvate + ATP (catalyzed by pyruvate kinase); and pyruvate + NADH + H⁺ \leftrightarrow lactate + NAD⁺ (catalyzed by lactate dehydrogenase).

In a 75- μ l reaction, we added 0.05 M Tris pH 7.2, 1 mM dithiothreitol, 2.5 mM MgCl₂, 5 mM ATP, 0.18 mM NADH, 0.21 mM phosphoenolpyruvate, 2.4 μ g pyruvate kinase and 1.5 μ g lactate dehydrogenase in H₂O (Sigma). Pyruvate kinase and lactate dehydrogenase were added in excess such that they were not rate-limiting (Supplementary Fig. 3e). Thymidine concentrations varied between 0.1 mM and 1.5 mM, and each reaction contained of 13 μ g of Tdk. Reactions were performed in triplicate. We measured the loss of NADH by measuring absorbance at 340 nm at 37 °C at 30 s intervals for 10–30 min.

GlpK activity was measured using a spectrophotometric assay similar to that described previously¹⁴. Reaction schema: glycerol + ATP \leftrightarrow ADP + glycerol-3-phosphate (catalyzed by GlpK); ADP + phosphoenolpyruvate + H⁺ \leftrightarrow pyruvate + ATP (catalyzed by pyruvate kinase); and pyruvate + NADH + H⁺ \leftrightarrow lactate + NAD⁺ (catalyzed by lactate dehydrogenase).

In a 75- μ l reaction, we added 0.05 M Tris pH 7.2, 3.33 mM glycerol, 0.1 M KCl, 5.25 mM phosphoenolpyruvate, 2.5 mM MgSO₄, 0.2 mM NADH, 2.25 μ g pyruvate kinase and 1.125 μ g lactate dehydrogenase in H₂O (Sigma). Pyruvate kinase and lactate dehydrogenase were added in excess such that they were not rate-limiting (Supplementary Fig. 3f). ATP concentrations varied between 0.033 mM and 1 mM, and each reaction contained of 1.8 μ g of GlpK. Reactions were performed in triplicate. We measured the loss of NADH by measuring absorbance at 340 nm at 37 °C at 30 s intervals for 10–30 min.

Pdp activity was measured using a spectrophotometric assay similar to that described in ref. 15. Reaction schema: deoxyuridine + phosphate \leftrightarrow deoxyribose-1-phosphate + uracil (catalyzed by Pdp).

In a 400- μ l reaction, we added 10 mM Tris pH 7.3, 10 mM phosphate pH 7.3 and 1 mM EDTA in H₂O. Deoxyuridine (Sigma) concentrations varied between 1.25 mM and 12.5 mM. Each reaction contained of 1 μ g of Pdp and was conducted at 37 °C for 9 min. At 45-s intervals, we added 70 μ l of 0.5 M NaOH to 30 μ l of reaction mix to stop the reaction. We determined uracil production by measuring absorbance at 290 nm.

Blank controls were performed for all reactions with H₂O instead of enzyme. NADH and uracil concentrations were determined from measurements of absorbance at 340 nm and 290 nm, respectively, using NADH and uracil standard curves. The maximal slope of each reaction curve was used to determine its velocity, and Hanes-Woolf plots were used to determine the v_{\max} and k_{cat} (Fig. 3a–c). Hanes-Woolf results were compared to Michaelis-Menten nonlinear regression results (Supplementary Fig. 3g,h). Both methods yielded comparable results.

Comparison of experimental data and model predictions. The following statistical measures were taken in analyzing the results shown in Figures 1b and 3e: at least six replicates were performed for each gene disruption-specific growth rate measurement, and 15 replicates were performed for the wild type. At least five simulations were run for each model prediction, and 128 simulations were run for the wild type. A heteroskedastic two-tailed *t*-test was performed between each set of experimental measurements and model predictions. We considered experimental and model results to be significantly different if *P* values were ≤ 0.01 . Owing to the small sample size, we wanted to be sure that our results were not biased by the distributions of the data or by extreme outliers. We performed a nonparametric Wilcoxon rank-sum test (also with cutoff of $P \leq 0.01$), which identified the same set of gene ‘hits’. Finally, from the list of genes with $P \leq 0.01$ (18 genes), we only considered those that were over or underpredicted by at least 20% (14 genes).

Linear regression of kinetic assay data. The following statistical measures were taken in computing the results of Figure 3a–c: kinetic reactions were performed in triplicate for seven substrate concentrations for each enzyme. A linear regression was fit to the data, and 99% confidence intervals were determined using the standard error of the slope and a *t* distribution obtained using $\alpha = 0.01$ and degrees of freedom = $n - 2 = 19$.

Enzyme quantification and k_{cat} range calculations. Isolated enzymes were quantified by SDS electrophoresis against known quantities of BSA. Band volumes were quantified using Quantity One v.4.6.9 software (intensity \times area). Linear regressions of the BSA standard curve were used to determine the isolated enzyme concentration. 95% confidence intervals of the linear regressions were determined using the standard errors of the slope and intercept and *t* distributions obtained using $\alpha = 0.05$ and degrees of freedom = $n - 2$ (Supplementary Fig. 3a–c). The lower enzyme concentration bound and upper v_{\max} bound for each enzyme was used to calculate the upper bound of the k_{cat} , and the upper enzyme concentration bound, and lower v_{\max} bound for each enzyme was used to calculate the lower bound of the k_{cat} (Supplementary Fig. 3d).

The final predicted values of k_{cat} used to constrain the whole-cell model were 0.215 s⁻¹ for Tdk, 0.5 s⁻¹ for Pdp and GlpK = 0.46 s⁻¹

for GlpK. The measured k_{cat} values used were 0.215 s^{-1} for Tdk, 78.1 s^{-1} for Pdp and 0.80 s^{-1} for GlpK (**Fig. 3e**). The k_{cat} values were input into the whole-cell model and compared to the experimentally measured specific growth rates and model predictions with original k_{cat} values. P values were determined by two-tailed t -test, $P \leq 0.01$.

Flux balance analysis. Flux balance analysis (FBA) has been used to make predictions of cellular growth rates based on a given metabolic network and environmental conditions⁷. However, other studies have noted the difficulty in quantitatively predicting the short-term effects of gene deletion on cell growth using FBA¹⁶. To test the capacity of FBA to quantitatively predict phenotypes of single-gene disruption strains for the *M. genitalium* metabolic network, we analyzed phenotypes of single-gene disruption strains of the metabolic genes in the same data set using FBA. We found that these predictions fell into only two categories: either zero growth rate or growth rate essentially similar to that of the wild type (**Supplementary Fig. 1a**). In contrast, the whole-cell model predictions included specific growth rates across the range of 0–115% of the growth rate of the wild type (**Supplementary Fig. 1b**).

The distribution was more descriptive than FBA, even in the case where only metabolic genes were considered. This most likely stemmed from two causes: first, the variation near to the growth rate similar to that of the wild type arose predominantly from the stochastic aspects of the whole-cell model; and second,

predicted specific growth rates more distant from that of the wild type were due to the substantial constraints on the whole-cell model's metabolic network. Specifically, the metabolic module of the whole-cell model was solved using a similar linear optimization strategy to FBA but with 63% of the catalysis reactions constrained by rate parameters as opposed to none of the catalysis reactions typically being constrained in FBA studies^{2,5}. The tight, detailed constraints on almost every metabolic reaction in the whole-cell model arise from a combination of many cellular processes in the whole-cell framework including transcription, tRNA aminoacylation, translation, protein processing and modification, protein translocation and folding, and macromolecular complexation. Previous studies have shown that the addition of new constraints to FBA improves predictive ability⁸, and our comparison underscores that such constraints may be essential to make accurate quantitative predictions about cellular growth rates. We conclude that the quantitative specific growth rates and hypotheses presented here required the use of the whole-cell model and would not have been achieved by FBA alone.

12. Gibson, D.G. *et al. Nat. Methods* **6**, 343–345 (2009).
13. Schelling, P., Folkers, G. & Scapozza, L. *Anal. Biochem.* **295**, 82–87 (2001).
14. Lester, L.M., Rusch, L.A., Robinson, G.J. & Speckhard, D.C. *Biochemistry* **37**, 5349–5355 (1998).
15. Leer, J.C., Hammer-Jespersen, K. & Schwartz, M. *Eur. J. Biochem.* **75**, 217–224 (1977).
16. Fong, S.S. & Palsson, B.O. *Nat. Genet.* **36**, 1056–1058 (2004).